PERGAMON

International Journal of Solids and Structures 38 (2001) 8547–8562

INTERNATIONAL JOURNAL OF SOLIDS and STRUCTURES

www.elsevier.com/locate/ijsolstr

Simulation of fiber debonding with friction in a model composite pushout test

G. Lin [a], P.H. Geubelle [a,b,*], N.R. Sottos [c]

[a] *Center for the Simulation of Advanced Rockets, University of Illinois at Urbana-Champaign, Urbana, IL 61801, USA*
[b] *Department of Aeronautical and Astronautical Engineering, University of Illinois at Urbana-Champaign, Urbana, IL 61801, USA*
[c] *Department of Theoretical and Applied Mechanics, University of Illinois at Urbana-Champaign, Urbana, IL 61801, USA*

Received 9 November 1998

Abstract

The interface failure observed in quasi-static fiber pushout tests performed on a model fiber-reinforced composite is simulated using a cohesive volumetric finite element scheme. The numerical analysis is conducted under axisymmetric condition. The debonding process is captured with the aid of intrinsic rate-independent cohesive elements. The augmented Lagrangian approach is used to solve the frictional contact between the crack faces. The numerical method is first applied to a model polyester/epoxy system, showing excellent agreement with the experimentally obtained load-deflection curve and with the observed evolution of the debonding length. The numerical scheme is then further applied in a parametric study of the effects of the friction coefficient, the interfacial bond strength and the process-induced residual stresses on the fiber–matrix interface failure process. © 2001 Elsevier Science Ltd. All rights reserved.

Keywords: Fiber pullout; Fiber pushout; Friction; Fiber reinforced composite; Cohesive zone model; Finite elements

---

1. Introduction

When a crack propagates in a composite material in a direction perpendicular to that of the reinforcing fibers, the failure process is quite complex and typically involves matrix cracking, fiber/matrix debonding, fiber pullout and fiber breakage. Of these four failure mechanisms, the fiber/matrix debonding and the frictional fiber pullout are generally considered as the most important source of energy dissipation and have therefore been the focus of the majority of research efforts dedicated to that topic.

To better characterize these two failure processes, several researchers have conducted fiber pullout and pushout experiments on a model composite (Fig. 1) involving a single fiber composite system. The fiber diameter is chosen one to three orders of magnitude larger than that of the actual composite reinforcement to allow for a better control and visual analysis of the failure process. In these experiments, the "macro-fiber" is slowly pulled or pushed out of the surrounding matrix (Bowling and Groves, 1979; Atkinson et al.,

---

[*] Corresponding author. Present address: 306 Talbot Laboratory, 104 S. Wright Street, Urbana, IL 61801, USA. Tel.: +1-217-244-7648; fax: +1-217-244-0720.

E-mail address: geubelle@uiuc.edu (P.H. Geubelle).

PII: S0020-7683(01)00085-3

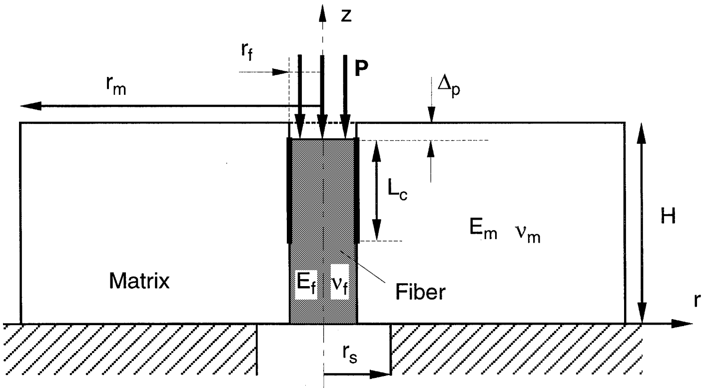

Fig. 1. Schematic of a pushout test of a model composite system.

1982; Khanna and Shukla, 1994; Tsai and Kim, 1996; Bechel and Sottos, 1998a,b,c). The critical interface parameters, such as the fracture toughness and the coefficient of friction, are then extracted from the evolution of the load applied on the fiber (P) and the resulting displacement of the pushout/pullout tool (Δ_p), and from observations of the propagation of the debonding front. A typical force–displacement curve obtained for a pushout test is shown in Fig. 2. After an initial stage in which the specimen settles on its support, a linear response corresponding to perfect fiber/matrix bonding is measured (stage I). Then, as the load increases, a crack initiates from the top of the specimen and starts to propagate along the interface, leading to a non-linear force/displacement relation (stage II). The debonding process is initially stable; but, as the crack length reaches a critical value, the failure process becomes unstable and leads to a sudden complete debonding of the fiber from the matrix. This instability is followed by the frictional sliding of the fiber out of the surrounding matrix (stage III).

Although the above description is representative of many experiments, it has to be modified in many situations to account for variations in the debonding and sliding events. For example, for a range of material systems involving a very large stiffness mismatch, the crack does not initiate from the top surface of the specimen, but from the bottom part instead (Bechel, 1997; Bechel and Sottos, 1998a,c). Another example concerns the type of debonding and sliding process: it can be continuous as a crack initiates from one end of the fiber and progressively expands along the whole fiber length (Bechel and Sottos, 1998a; Tsai

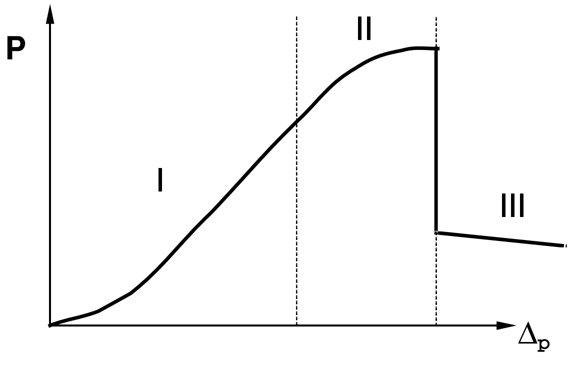

Fig. 2. A typical load–deformation curve obtained in a pushout test.

and Kim, 1996), or discontinuous as a dislocation-like sliding zone propagates along the fiber/matrix interface in a manner similar to that of Schallamach waves observed in rubbery materials sliding over a hard surface (Kendall, 1975; Tsai and Kim, 1996). Depending on the fiber surface roughness and the amplitude of the compressive residual stresses acting along the interface, the sliding process (stage III) can also be either continuous, or involve a stick-slip process.

Various analytical investigations have been conducted to interpret these experiments. One of the most successful approaches is based on the shear lag theory (Shetty, 1988; Hutchinson and Jensen, 1990; Kerans and Parthasarathy, 1991; Liang and Hutchinson, 1993). This approach involves the following assumptions: the axial load acting on the fiber is transmitted to the matrix solely through shear stresses acting on the interface; the surface or end effects are neglected; the compressive (residual) radial stress is assumed to be uniform; and the debonding front initiates from the top of the sample, not from the bottom. Although somewhat restricted by these assumptions, this analytical treatment of the fiber pullout/pushout tests has the major advantage of providing a closed-form solution of the problem, allowing a quick characterization of the effects of the many parameters entering the problem such as the fiber length and radius, the process-induced residual stress, the friction coefficient and the fiber/matrix modulus mismatch. However, as shown by Bechel and Sottos (1998a,b), by neglecting the end effects, the shear-lag theory tends to underestimate the debond length observed in the second stage of the experiment, and thereby to over-predict the interface fracture toughness. However, the shear lag is in some cases successful in extracting the friction coefficient from the initial part of the stage III force–displacement curve.

Other analytical techniques have also been used to support the fiber pullout/pushout experiments. Liang and Hutchinson (1993) used the finite element method to determine the range of validity of the shear lag method. Kallas et al. (1992) also adopted the finite element scheme to compute the stress distribution corresponding to the pushout test when the fiber and the matrix are fully bonded. The same numerical method was also used by Beckert and Lauke (1995) and by Chandra and Ananth (1995) to extract interface failure properties. Freund (1991) solved the integro-differential equation governing the axial stress in the fiber to study the sliding of a fiber in a hole in an elastic material. In their finite element simulation of a rigid rod pulled out of an elastic matrix, Povirk and Needleman (1993) used a rate- and state-dependent friction model to capture the aforementioned dislocation-like frictional sliding of the fiber. The effect of more complex friction models is also the topic of the analytical investigations presented by Tsai and Kim (1996).

The emphasis of the numerical work summarized hereafter is however somewhat different: while the majority of the existing analytical work has focused on the frictional sliding of the debonded fiber (stage III), we aim at capturing the progressive failure of the fiber/matrix interface and the associated frictional contact of the newly created fracture surfaces (stage II). Unlike the shear lag approach, the method used in this work captures the stress concentrations associated with the end effects and with the advancing crack front. Although the method can be applied to both fiber pullout and pushout problems, we primarily simulate the failure events associated with the fiber pushout test to allow for comparison with a set of very detailed experimental observations recently obtained by Bechel and Sottos (1998a,b,c).

The method used in this analysis is a special axisymmetric version of the cohesive/volumetric finite element (CVFE) scheme, which has recently been used by many research groups in the modeling of various quasi-static (Needleman, 1987; Tvergaard and Hutchinson, 1992; Lin et al., 1997; Lin et al., 1998) and dynamic (Camacho and Ortiz, 1996; Needleman, 1997; Geubelle and Baylor, 1998) fracture events involving the initiation, propagation and/or arrest of cracks. The particular implementation of the CVFE scheme used in the present study involves a bilinear rate-independent intrinsic cohesive model, coupled with a frictional contact element.

The paper is organized as follows: the numerical scheme and the problem description are summarized in the next section, followed, in Section 3, by a comparison between experimental observations and numerical results for a model polyester/epoxy composite system. Section 3 also contains a parametric study of the effect on the failure process of some important quantities such as the fracture energy, the residual stresses, the friction coefficient, etc. These results are further discussed in Section 4, which also contains a brief presentation of a fiber pullout simulation.

2. Problem formulation

2.1. Finite element formulation

The finite element analysis is based on an Eulerian formulation due to McMeeking and Rice (1975). Attention is confined to quasi-static deformations, and, with body forces neglected, the principle of virtual work is written as

$$\int_V \left[\tau^*_{ij}\ \delta D_{ij} - \frac{1}{2}\sigma_{ij}\ \delta(2D_{ik}D_{kj} - v_{k,i}v_{k,j})\right] \mathrm{d}V + \int_{S_{\text{int}}} \delta\dot{\phi}\, \mathrm{d}S = \int_{S_{\text{ext}}} \dot{T}^i \delta v_i\, \mathrm{d}S, \tag{1}$$

where all integrations are performed in the current equilibrium configuration; V, S_{int} and S_{ext} denote the volume, interfacial surfaces and external surfaces, respectively; τ_{ij} is the Kirchhoff stress and τ^*_{ij} its Jaumann rate; σ_{ij} denotes the Cauchy stress; $\dot{T}^i$ represents the nominal surface traction rates based on the current surface area; u_i and v_i are the displacement and displacement rate fields, respectively; $v_{i,j}$ corresponds to $\partial v_i/\partial x_j$, where x_i is position vector of a material point in the current state. Finally, D_{ij} is rate of deformation tensor defined as

$$D_{ij} = (v_{i,j} + v_{j,i})/2. \tag{2}$$

The virtual interfacial work $\delta\phi$ appearing in Eq. (1) is specified next.

2.2. The cohesive zone model

The cohesive zone model consists of a constitutive relation between the tractions $\boldsymbol{T}$ acting on the interface and the corresponding interfacial separation Δ (displacement jump across the interface). In the present work, we use an intrinsic cohesive failure model, in which, as the interface separates, the magnitude of $\boldsymbol{T}$ increases, reaches a maximum and then progressively falls to zero as complete separation occurs. Various interfacial constitutive relations exhibiting this qualitative behavior can be constructed: exponential (Needleman, 1987, 1997), trapezoidal (Tvergaard and Hutchinson, 1992) and bilinear (Geubelle and Baylor, 1998) to cite a few examples.

In the present study, we modify the rate-independent bilinear cohesive failure model used by Geubelle and Baylor (1998) to account for frictional contact between the newly created fracture surfaces. Friction sliding is assumed to obey the Coulomb friction law (with a constant friction coefficient μ), yielding the following relation between the normal (T_{n}) and tangential (T_{t}) cohesive tractions and the normal (Δ_{n}) and tangential (Δ_{t}) displacement jumps:

$$T_{\text{n}} = \begin{cases} \frac{\sigma_{\max}}{\delta_{\max}}\,\delta_{\text{n}}, & \text{for } \delta \leqslant \delta_{\max} \\ \frac{\sigma_{\max}}{\delta}\,\frac{1-\delta}{1-\delta_{\max}}\,\delta_{\text{n}}, & \text{for } \delta > \delta_{\max} \end{cases} \tag{3}$$

$$T_{\text{t}} = \begin{cases} \frac{\sigma_{\max}}{\delta_{\max}}\,\frac{\Delta^{\text{c}}_{\text{n}}}{\Delta^{\text{c}}_{\text{t}}}\,\delta_{\text{t}}, & \text{for } \delta \leqslant \delta_{\max} \\ \frac{\sigma_{\max}}{\delta}\,\frac{1-\delta}{1-\delta_{\max}}\,\frac{\Delta^{\text{c}}_{\text{n}}}{\Delta^{\text{c}}_{\text{t}}}\,\delta_{\text{t}}, & \text{for } \delta > \delta_{\max} \end{cases} \tag{4}$$

for $\delta_{\text{n}} > 0$, and

$$T_{\mathrm{t}} = \begin{cases} \frac{\sigma_{\max}}{\delta_{\max}} \frac{\Delta_{\mathrm{n}}^{\mathrm{c}}}{\Delta_{\mathrm{t}}^{\mathrm{c}}} \delta_{\mathrm{t}}, & \text{for } \delta \leq \delta_{\max} \\ \frac{\sigma_{\max}}{\delta} \frac{1-\delta}{1-\delta_{\max}} \frac{\Delta_{\mathrm{n}}^{\mathrm{c}}}{\Delta_{\mathrm{t}}^{\mathrm{c}}} \delta_{\mathrm{t}}, & \text{for } \delta > \delta_{\max} \\ \mathrm{sign}(\Delta_{\mathrm{t}}) \mu T_{\mathrm{n}}, & \text{for } |T_{\mathrm{t}}| < \mu |T_{\mathrm{n}}| \end{cases} \tag{5}$$

for $\delta_{\mathrm{n}} = 0$. In the latter case, the normal traction across the interface is calculated by a contact algorithm (see below) to enforce the condition $\delta_{\mathrm{n}} = 0$.

In Eqs. (3)–(5), δ_{n}, δ_{t} and δ respectively denote the nondimensional normal, tangential and total displacement jumps, defined by

$$\delta_{\mathrm{t}} = \frac{\Delta_{\mathrm{t}}}{\Delta_{\mathrm{t}}^{\mathrm{c}}}, \delta_{\mathrm{n}} = \frac{\Delta_{\mathrm{n}}}{\Delta_{\mathrm{n}}^{\mathrm{c}}}, \delta = \sqrt{\delta_{\mathrm{t}}^2 + \delta_{\mathrm{n}}^2}, \tag{6}$$

where $\Delta_{\mathrm{n}}^{\mathrm{c}}$ and $\Delta_{\mathrm{t}}^{\mathrm{c}}$ are the critical normal and tangential separations at which complete separation is assumed.

The variation of the normal and tangential traction components with respect to Δ_{n} and Δ_{t} corresponding to pure opening ($\Delta_{\mathrm{t}} = 0$) and pure shear separation ($\Delta_{\mathrm{n}} = 0$) are shown in Fig. 3a, b. The maximum value of T_{n} is $\sigma_{\max}$ and occurs at $\Delta_{\mathrm{n}} = \delta_{\max}\Delta_{\mathrm{n}}^{\mathrm{c}}$. The maximum value of $|T_{\mathrm{t}}|$ is $\tau_{\max}$ given by

$$\tau_{\max} = \sigma_{\max}\Delta_{\mathrm{n}}^{\mathrm{c}}/\Delta_{\mathrm{t}}^{\mathrm{c}}, \tag{7}$$

and is attained at $|\Delta_{\mathrm{t}}| = \delta_{\max}\Delta_{\mathrm{t}}^{\mathrm{c}}$. The normal ($\Gamma_{\mathrm{n}}$) and tangential ($\Gamma_{\mathrm{t}}$) works of separation per unit area of interface are given by

$$\Gamma_{\mathrm{n}} = \frac{\sigma_{\max}\Delta_{\mathrm{n}}^{\mathrm{c}}}{2}, \qquad \Gamma_{\mathrm{t}} = \frac{\tau_{\max}\Delta_{\mathrm{t}}^{\mathrm{c}}}{2}. \tag{8}$$

Note that Eqs. (7) and (8) imply that $\Gamma_{\mathrm{n}} = \Gamma_{\mathrm{t}}$. Although not really required, this assumption greatly simplifies the implementation of the quasi-static cohesive volumetric finite element scheme, since it results in a symmetric stiffness matrix. As the failure process observed in the fiber pushout problem is almost exclusively in shear and involves an almost negligible contribution from the opening (normal) mode, this assumption is not expected to have any impact on the solution.

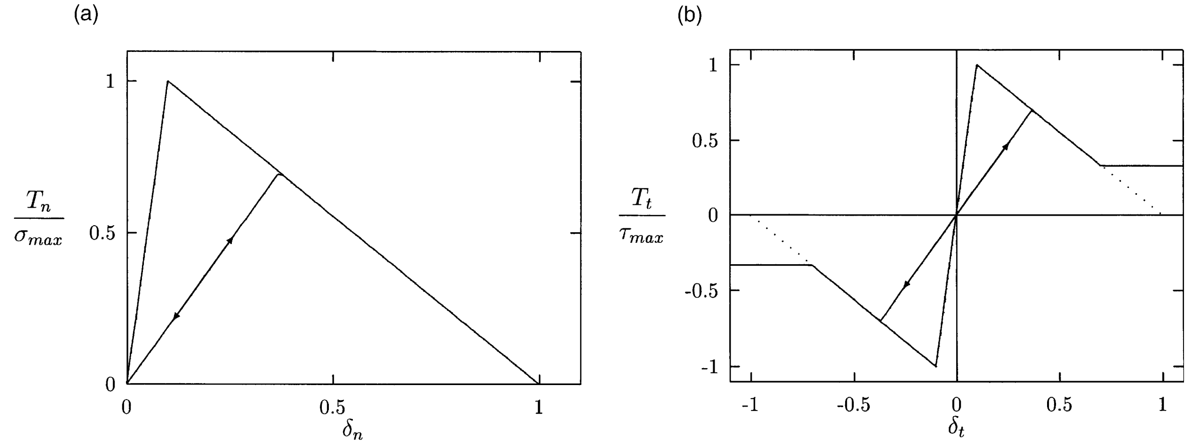

Fig. 3. Cohesive law. (a) Normal traction T_{n} as a function of the normal separation δ_{n} for $\delta_{\mathrm{t}} = 0$; (b) shear traction T_{t} versus shear separation δ_{t} for $\delta_{\mathrm{n}} = 0$. The solid and dotted curves correspond to a shear cohesive failure for a frictional ($\mu > 0$) and frictionless ($\mu = 0$) contact, respectively.

As can be seen from Eqs. (3)–(5), the response at each point of along interface is characterized by four parameters: $\delta_{\max}$, $\sigma_{\max}$, Δ_t^c and Δ_n^c. The number of parameters can be reduced to three since the results are almost insensitive to $\delta_{\max}$ as long as the stiffness of interface elements is larger than that of the surrounding volumetric elements.

To account for frictional contact between the newly created fracture surfaces, the Kuhn–Tucker conditions for Coulomb friction are specified for the part of interface that has debonded:

$$\Phi = |T_t| - \mu |T_n| \leqslant 0, \tag{9}$$

$$\dot{u}_t = \xi \frac{\partial}{\partial T_t} \Phi, \tag{10}$$

$$\xi \geqslant 0, \tag{11}$$

$$\xi \Phi = 0, \tag{12}$$

where μ is the coefficient of friction. Eqs. (10) and (11) mandate that sliding occurs in the direction opposite that of the applied shear traction, and Eq. (12) enforces the condition that slip may only take place when $\Phi = 0$, i.e., when $|T_t| = \mu |T_n|$. If $|T_t| < \mu |T_n|$, then $\dot{u}_t = 0$ and stick conditions are assumed along the interface.

The interfacial component of the virtual work is then written as

$$\int_{S_{\mathrm{int}}} \delta \dot{\phi} \, \mathrm{d}S = \int_{S_{\mathrm{int}}} \left[\frac{\partial T_n}{\partial \Delta_n} \dot{\Delta}_n \delta \dot{\Delta}_n + \frac{\partial T_n}{\partial \Delta_t} \dot{\Delta}_n \delta \dot{\Delta}_t + \frac{\partial T_t}{\partial \Delta_n} \dot{\Delta}_t \delta \dot{\Delta}_n + \frac{\partial T_t}{\partial \Delta_t} \dot{\Delta}_t \delta \dot{\Delta}_t \right] \mathrm{d}S. \tag{13}$$

In conclusion, the interface is discretized in a series of interface elements, henceforth referred to as cohesive elements. Prior to interface debonding, Eqs. (3)–(5) are used to describe the evolution of the normal and tangential tractions acting across the interface elements for which $\Delta_n > 0$ and evolution of the tangential traction component where surfaces of cohesive elements are in contact ($\Delta_n = 0$). The augumented Lagrangian treatment (Simo and Laursen, 1992) is used to constrain the frictional sliding along the debonded interface and to enforce the appropriate contact condition. It has to be noted however that the enforcement of the contact condition along the sliding cohesive elements is only local, as contact is only checked between originally adjacent volumetric elements. While this approach is not adequate to capture the third stage of the pushout experiment characterized by substantial relative motion of the fiber and the matrix, it is expected to be applicable to simulate the progressive failure process taking place during stage II.

2.3. Finite element model

A sketch of the model composite specimen, which includes the various quantities defining the geometry and the material properties of the fiber and the matrix, has been presented in Fig. 1. As indicated earlier, the finite element analysis is conducted under axisymmetric condition. Perfect bonding between the matrix and the fiber is assumed at the beginning of the simulation. Frictionless contact is assumed between the punch and the fiber, and between the bottom side of the matrix and the support. The analysis is performed in two steps: in the first one, the process-induced residual stresses associated with the chemical shrinkage experienced by the matrix are computed by treating the shrinkage strains as residual thermal strains present in the matrix. In the second step, the axial punch displacement Δ_p is applied on the top of the fiber, and the corresponding punch force P is determined by summing the reaction force on the punch nodes.

The finite element mesh used in the majority of the simulations will be shown later in its deformed configuration in Fig. 6. It consists of 1024 four-noded volumetric elements and 104 four-noded cohesive

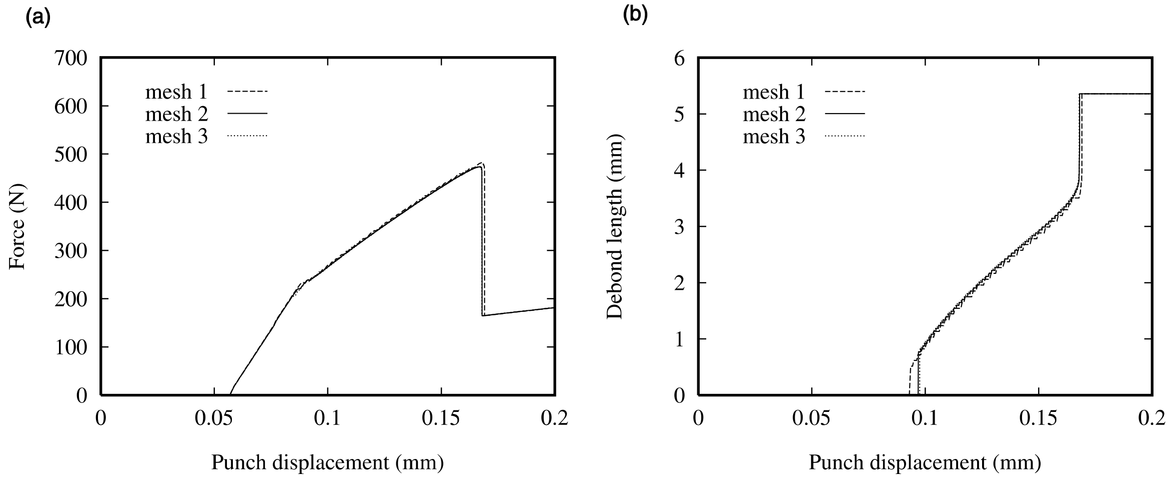

Fig. 4. Effect of the mesh size on the finite element predictions of the punch load versus displacement curve (a), and of the evolution of the debond length (b).

elements evenly distributed along the fiber/matrix interface, for a total of 1268 nodes. To examine the effect of the mesh size on the solution, three discretizations have been considered: the mesh shown in Fig. 6 is labeled Mesh 2; Mesh 1 is twice as coarse, with only 52 elements along the interface, and Mesh 3 is twice as fine with 208 interface elements. A comparison between the results obtained with these three dicretizations is presented in Fig. 4, showing almost perfect similarity both for the predicted punch force/displacement curve and for the evolution of the length of the debonding crack.

In the next section, the effect of various parameters such as $\sigma_{\max}$, E_f/E_m and μ on the debonding and frictional sliding processes are investigated. We do not however examine the effect of the specimen dimensions, which are henceforth chosen to match those used in the experiments performed by Bechel and Sottos (1998a): fiber radius $r_f = 0.95$ mm, specimen radius $r_m = 4.3$ mm, specimen thickness $H = 5.36$ mm and support inner radius $r_s = 1.025$ mm.

3. Results

3.1. Comparison between experiment results and numerical predictions

In order to determine whether the cohesive/volumetric finite element scheme can adequately capture the failure process associated with the second stage of the pushout test, we first attempt to simulate Bechel and Sottos' (1998a) experiments performed on a polyester/epoxy model composite. The elastic properties of the constituents are $E_f = 2500$ N/mm^2, $\nu_f = 0.35$, $E_m = 4000$ N/mm^2 and $\nu_m = 0.33$.

The experimentally measured chemical matrix shrinkage strain is given by $\epsilon_{th} = -0.0022$. Bechel and Sottos (Bechel, 1997) extracted the friction coefficient, $\mu = 0.52$, from Stage II data and the mode II interface fracture toughness, $G_{II}^c = 0.11$ N/mm, from Stage III measurements. Since shear failure is by far the dominant failure mechanism in this case, it is assumed that Δ_n^c is equal to Δ_t^c.

This first set of simulations with the CVFE scheme constitutes therefore an excellent test for the numerical method, since we are left with a single parameter ($\sigma_{\max}$) to be determined to match the experimentally obtained punch force/displacement curve. It is found that a value of $\sigma_{\max}$ equal to 22 N/mm^2 provides the best match, as indicated in Fig. 5a. Note how precisely the numerical results capture both the

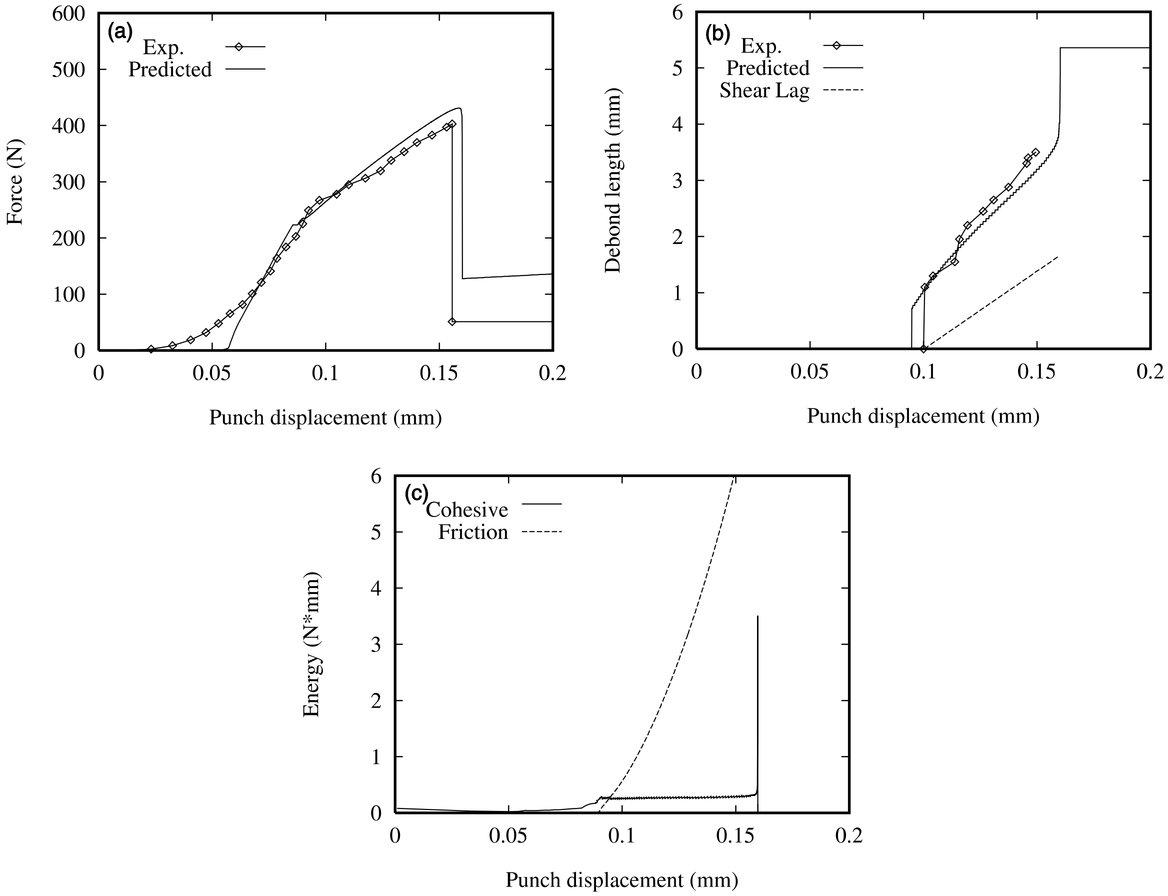

Fig. 5. Comparison between experimental measurements and numerical predictions for a pushout test performed on a polyester/epoxy model composite: (a) load versus punch displacement; (b) debonding length versus punch displacement; (c) cohesive and friction energies versus punch displacement.

shape of the nonlinear force/displacement curve associated with the debonding process and the onset of instability. Although these experimental results were not part of the curve fitting exercise, excellent agreement is also achieved between the numerical prediction (solid curve) and the experimental observations (solid curve with symbols) of the evolution of the debonding length, as indicated in Fig. 5b. A view of the deformed mesh corresponding to a debond length $L_c = 3$ mm is shown in Fig. 6. For comparison purpose, the debond length prediction obtained with the shear lag method (Bechel and Sottos, 1998a) is also presented in Fig. 5b. The inability of the shear lag approach to adequately capture the edge effects associated with the large shear stress concentration present along the edges of the fiber/matrix interface is clearly visible. The slope of the debond length versus punch displacement curve corresponding to the shear lag solution is also different from the experimental and numerical values.

An important advantage of the numerical analysis is its ability to provide an insight on the energetics of the failure process, and, in particular, on the relative importance of the energy dissipated in the cohesive failure itself compared to that dissipated in the frictional sliding. These two components of the energy are plotted in Fig. 5c as a function of the punch displacement. As expected, after initiation of the debonding, the cohesive fracture work (i.e., the energy that would be required at that stage of the experiment to further

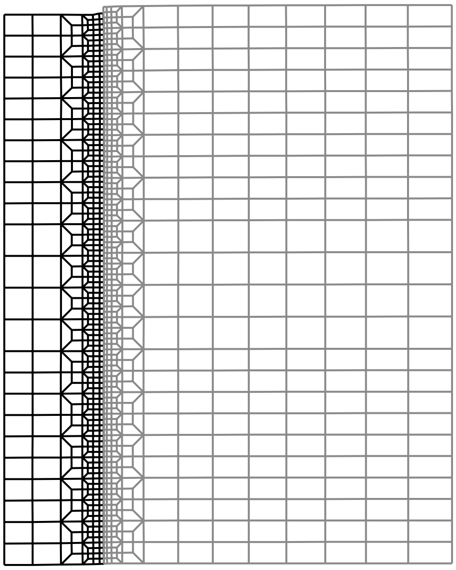

Fig. 6. Deformed mesh.

advance the crack by a small amount) remains constant prior to final complete debonding. In contrast, the frictional dissipative work increases dramatically as the crack length and the frictional shear stress increase, as described in the next section.

3.2. Parametric studies

Many parameters affect the overall load-deformation and fracture behavior of the composite. A dimensional analysis identifies the following nondimensional groups

$$\frac{L_\mathrm{c}}{r_\mathrm{f}} \quad \text{and} \quad \frac{P}{G_\mathrm{II}^\mathrm{c}} = fn\left(\frac{\Delta_\mathrm{p}}{r_\mathrm{f}}, \frac{\sigma_\mathrm{max} r_\mathrm{f}}{G_\mathrm{II}^\mathrm{c}}, \frac{E_\mathrm{f}}{E_\mathrm{m}}, \nu_\mathrm{f}, \nu_\mathrm{m}, \epsilon_\mathrm{th}, \mu, \frac{H}{r_\mathrm{f}}, \frac{r_\mathrm{m}}{r_\mathrm{f}}, \frac{r_\mathrm{s}}{r_\mathrm{f}}\right). \tag{14}$$

In this section, we systematically study the effects of some of the nongeometrical parameters, and, in particular, of the stiffness mismatch ($E_\mathrm{f}/E_\mathrm{m}$), friction coefficient (μ), matrix residual strain (ϵ_th) and interfacial strength (σ_max). Unlike in the previous section, our intent here is not to simulate a specific material system, but to provide some insights on the effect of the chosen parameters on the overall deformation behavior and failure process of the model composite. The results of a polyester/epoxy fiber composite shown in the previous section are taken as a reference and always denoted by a solid curve. Unless stated otherwise, the other parameters used in the following calculations are the same as those used in Section 3.1.

3.2.1. Effect of stiffness mismatch (E_f/E_m)

Experimental results (Bechel and Sottos, 1998a) have indicated that the fiber-to-matrix stiffness ratio ($E_\mathrm{f}/E_\mathrm{m}$) has a significant effect on the failure mechanism of the model composite, especially with regards to the appearence of a top versus bottom debond. This fact is confirmed in Fig. 7a, b, which respectively present the predicted punch load–displacement curve and the crack length evolution for four values of $E_\mathrm{f}/E_\mathrm{m}$.

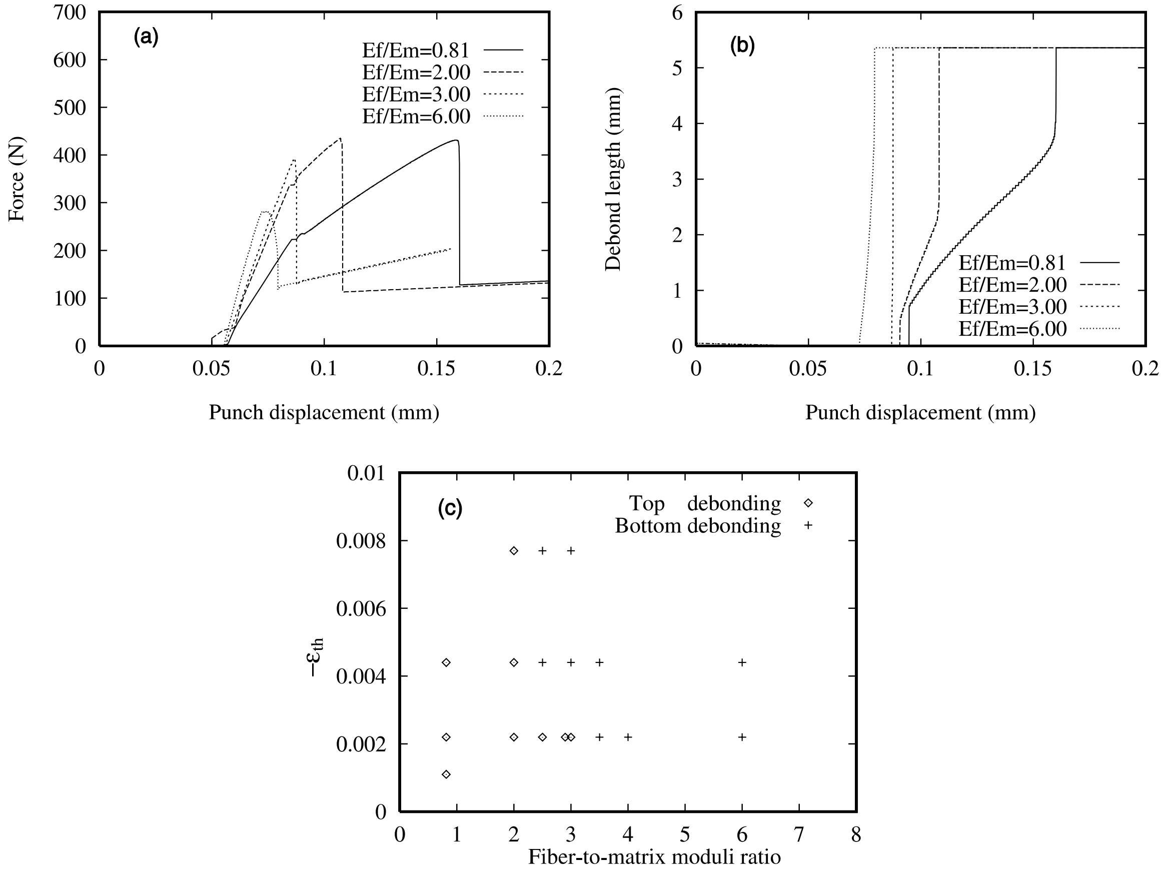

Fig. 7. Effect of the fiber-to-matrix modulus ratio E_f/E_m: (a) punch load versus displacement; (b) evolution of the debond length; (c) map of top and bottom debonding for various of E_f/E_m and ϵ_{th}. In (b), a top debond is predicted for the lower two values of E_f/E_m and a bottom debond for the other two values.

The maximum punch force P remains fairly constant (about 430 N) when $E_f/E_m \leqslant 3$ but begins to drop for higher values of the stiffness ratio. This behavior appears to be related to a transition in the crack initiation process: for $E_f/E_m \geqslant 4$, the debonding initiates at the bottom end of the fiber–matrix interface and advances upward until complete failure occurs. In contrast, for $E_f/E_m < 2$, a top debond is obtained. For the intermediate range of stiffness ratio ($2 < E_f/E_m < 4$), both types of crack initiation are predicted. All top debond cases involve quasi-exclusively mode II type of failure, as the crack faces are constantly in contact over their entire length. For the bottom debonding situations, some opening is observed and the failure process takes place under mixed mode conditions, especially for the initial stages of the interface debonding. However, prior to the complete debonding of the interface, the originally separated failure surfaces enter into contact and the later stages of the failure process take place under purely mode II conditions.

A map summarizing the combined effect of the residual strain and the modulus mismatch on the type of debond is presented in Fig. 7c, showing a trend very similar to that observed experimentally, as compiled by Bechel and Sottos (see Fig. 9 of Bechel and Sottos 1998a). As was the case in the experimental results, the type of failure (top versus bottom debond) seems to depend very little on the amplitude of the residual strain. Further comments on the effect of the residual strains are presented below.

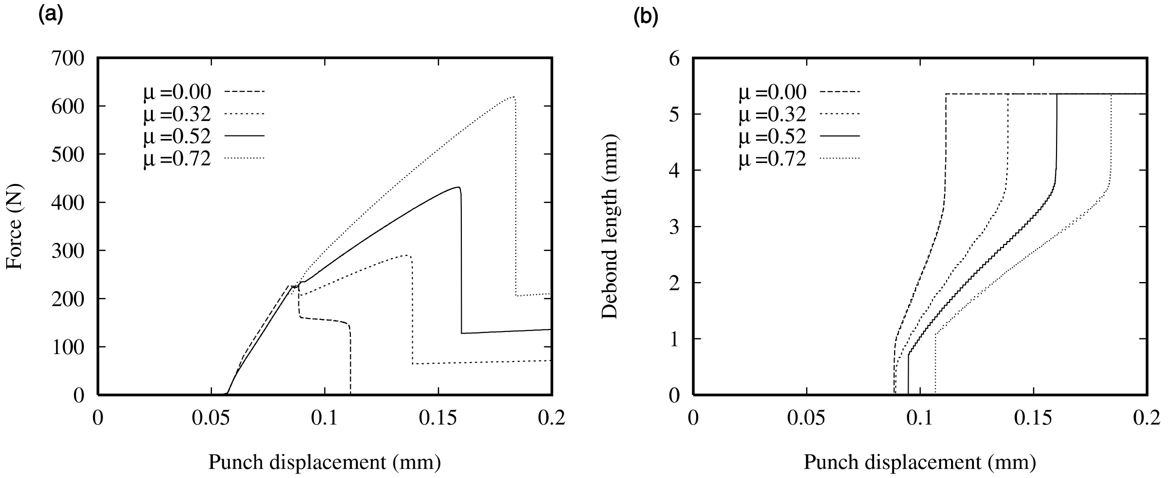

Fig. 8. Effect of friction coefficient μ on the numerical prediction of the punch load versus displacement curve (a), and of the debond length evolution (b).

3.2.2. *Effect of friction coefficient (μ)*

As discussed in Section 3.1, friction between the newly created crack faces plays a crucial role in the energetics of the overall failure process, especially for composite systems characterized by the presence of high compressive residual stress acting across the fiber/matrix interface. As seen in Fig. 8a which presents the predicted load versus punch displacement curves for four values of the friction coefficient ($\mu = 0$, 0.32, 0.52 and 0.72), it also plays a major role on the stability of the failure process by significantly increasing the load carrying and deformation capabilities of the composite specimen and by delaying the onset of catastrophic failure. The friction coefficient does not seem to affect the type of failure, however, as a top debond was observed in all four cases.

The predicted debond length versus punch displacement is shown in Fig. 8b. Increased friction significantly delays the interfacial debonding, confirming the results presented in the previous figure. Debonding initiation is associated with an approximate 1 mm pop-in (unstable debonding) for all cases. As the punch displacement Δ_p is further increased, the debond length increases almost linearly with Δ_p, with the slope strongly dependent on the friction coefficient. It is interesting to note, however, that while delaying the final unstable failure of the specimen by substantially increasing the load capability of the specimen, the friction coefficient does not appear to affect the value of the crack length at which instability is predicted to occur: in all cases, this crack length is approximately 3.7 mm.

3.2.3. *Effect of residual strain (ϵ_{th})*

Process-induced residual strains present in a composite are associated with the mismatch in coefficient of thermal expansion between the constituents and/or with the chemical shrinkage in the thermosetting matrix. Whatever their origin, they result in a larger relative contraction of the matrix and induce normal (compressive) and shear stresses along the interface. These pre-existing stresses, in turn, strongly affect the frictional sliding of the fiber, as illustrated in Fig. 9a, which displays the predicted punch load versus displacement curves for three thermal residual strain values, $\epsilon_{th} = -0.0011$, -0.0022, -0.0044.

An effect similar to that of the friction coefficient is observed, except with regards to the initiation phase: while the friction coefficient has (obviously) no effect on the value of the punch load at which the initial debonding front is predicted to appear, higher values of the residual strains delay the appearence of the initial unstable short crack, which signals the start of stage II of the experiment. The other effects of the

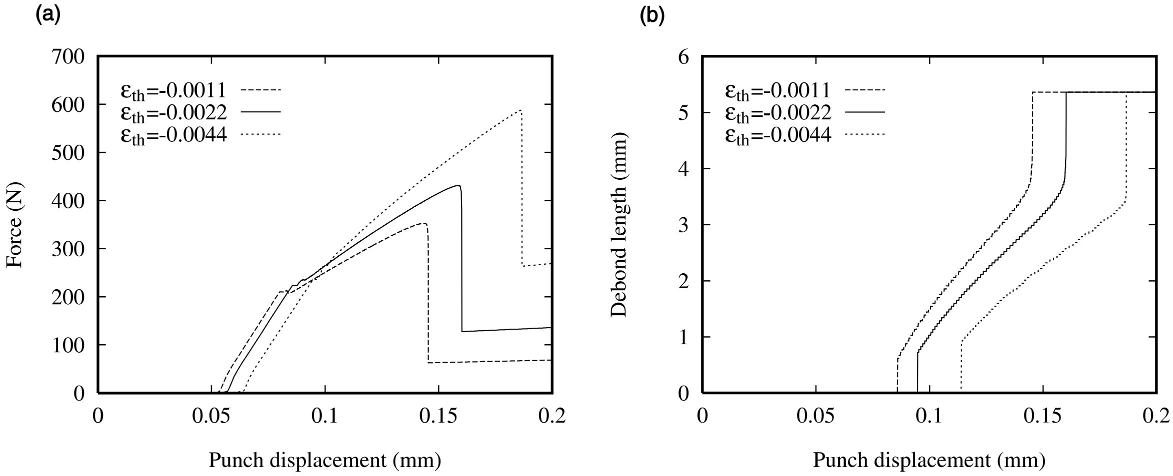

Fig. 9. Effect of the thermal residual strain ϵ_{th} on the force versus punch displacement curve (a), and on the crack propagation (b).

residual strain are similar to those associated with the friction coefficient: higher maximum load, delayed final instability and modified slope of the crack length versus punch displacement curve (Fig. 9b).

3.2.4. Effect of interfacial strength (σ_{max})

As discussed in Section 2.2, three parameters characterize the present cohesive failure model, i.e., σ_{max}, Δ_n^c and Δ_t^c. To limit the number of parameters, it has been assumed that $\Delta_n^c = \Delta_t^c$, which, as indicated earlier, is not expected to affect the simulation results since shear failure is by far the dominant mechanisms in the great majority of fiber pushout problems. This assumption leaves us with two parameters: σ_{max} and Δ_t^c. In this section, we examine the effect of the interfacial strength σ_{max} on the failure process, for a fixed value of the critical displacement jump $\Delta_n^c = \Delta_t^c = 0.01$ mm.

Fig. 10a, b show how σ_{max} affects the failure process by delaying the onset of stage II and by increasing the maximum load obtained just prior to the final unstable crack propagation. As expected, the frictional sliding is not affected by σ_{max} and the slope of the punch load versus displacement curve is the same in all three cases prior to debonding.

4. Discussion

The basic failure mechanism in brittle fiber/matrix composites involves: (1) brittle fracture of the fiber and the matrix, and (2) debonding and frictional sliding along the fiber/matrix interface. The present work has focused on the numerical simulation of the second mechanism. A simple rate-independent cohesive failure model coupled with a Coulomb friction model, allowing for the simulation of crack initiation and propagation under shear-dominated conditions has been incorporated in an axisymmetric finite element model of the pushout test performed on a model polyester/epoxy composite. Comparisons between the numerical prediction and the experimental data summarized in Fig. 5a, b indicate that the present model captures the observed failure process very well. By comparing the relative importance of the energy associated with the cohesive failure process and that dissipated in the frictional sliding of the crack faces (Fig. 5c), it can be concluded that the latter process plays by far the most important role in the composite overall fracture toughness.

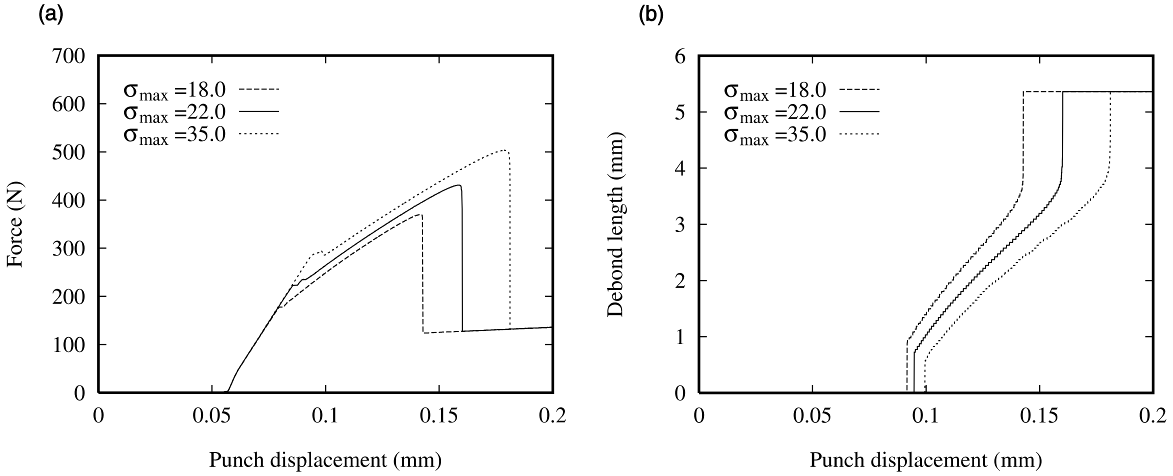

Fig. 10. Effect of the interfacial strength $\sigma_{\max}$ (given in MPa): (a) load versus punch displacement; (b) debonding length versus punch displacement.

Further insight on that process can be obtained from Fig. 11a, b, which respectively present the evolution of the distribution of shear (T_t) and radial (T_n) traction stresses acting along the interface for the polyester/epoxy composite discussed in Section 3.1 at several loading stages corresponding to debonding lengths $L_c = 1$, 2, 3 and 5.36 mm. Recall that the origin of the z-axis is located at the bottom side of the specimen, but the crack length L_c is measured from the top of the specimen. A very high friction-induced shear stress, higher than the shear stress computed in the cohesive elements located ahead of the debonding tip, is observed near the top end of the fiber/matrix interface. This frictional shear stress increases as the crack propagates downward, as the increasingly compressed fiber try to expand in the radial direction and is constrained by the surrounding matrix, itself shrinking under the effect of the residual strains.

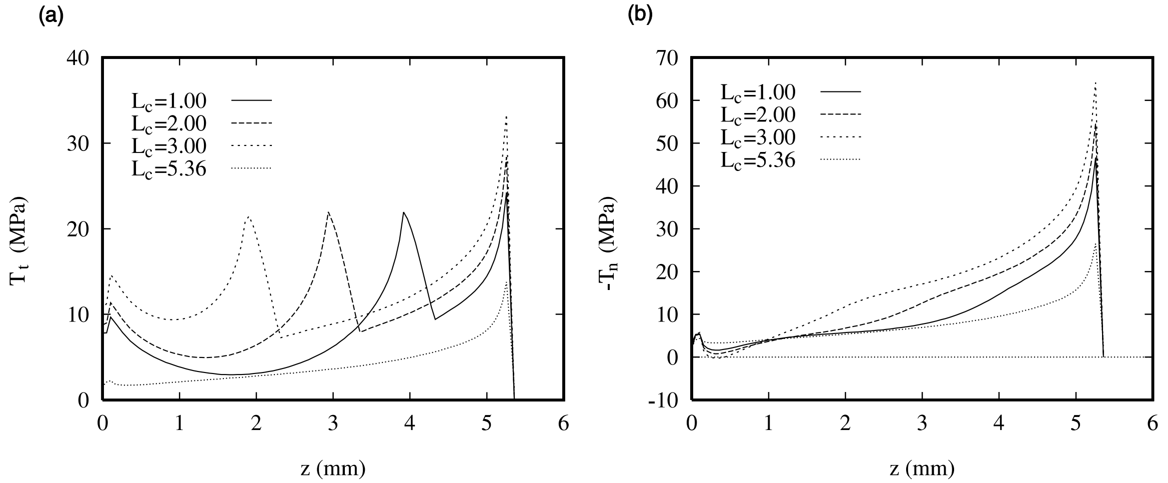

Fig. 11. Evolution of the interfacial stress distribution during the debonding process: (a) shear traction $T_t(z)$; (b) normal traction $T_n(z)$. The debond length L_c is given in mm.

This fact seems to indicate that the friction coefficient and the residual compressive radial stresses are the most important parameters affecting the overall fracture toughness of the composite. Both parameters result in a higher load carrying capacity and substantially delay the instability associated with the complete fiber–matrix interface debonding. However, by preventing the relative sliding of the crack faces, an excessive value of the friction stresses may result in a reduction of the extent of debonding which in turn may result in premature fiber or matrix fracture. This suggests that there exist an optimal friction level and an optimal value for the residual stresses which maximize the overall fracture toughness of the composite. Although the CVFE scheme used in the present study could also be used to model the brittle failure of the matrix and the fibers, the study of the transition between these different types of failure mechanisms is beyond the scope of the present work. Finally, while the correct characterization of friction sliding of a fiber embedded in a matrix remains an open issue, the present work based on a simple Coulomb friction law seems to reproduce the experiments quite well.

As a final illustration of the essential role of the frictional contact on the stability of the failure process, a comparison between fiber pushout and pullout tests is presented in Fig. 12, in terms of the punch force/displacement curve (Fig. 12a), debond length versus punch displacement curve (Fig. 12b) and distribution

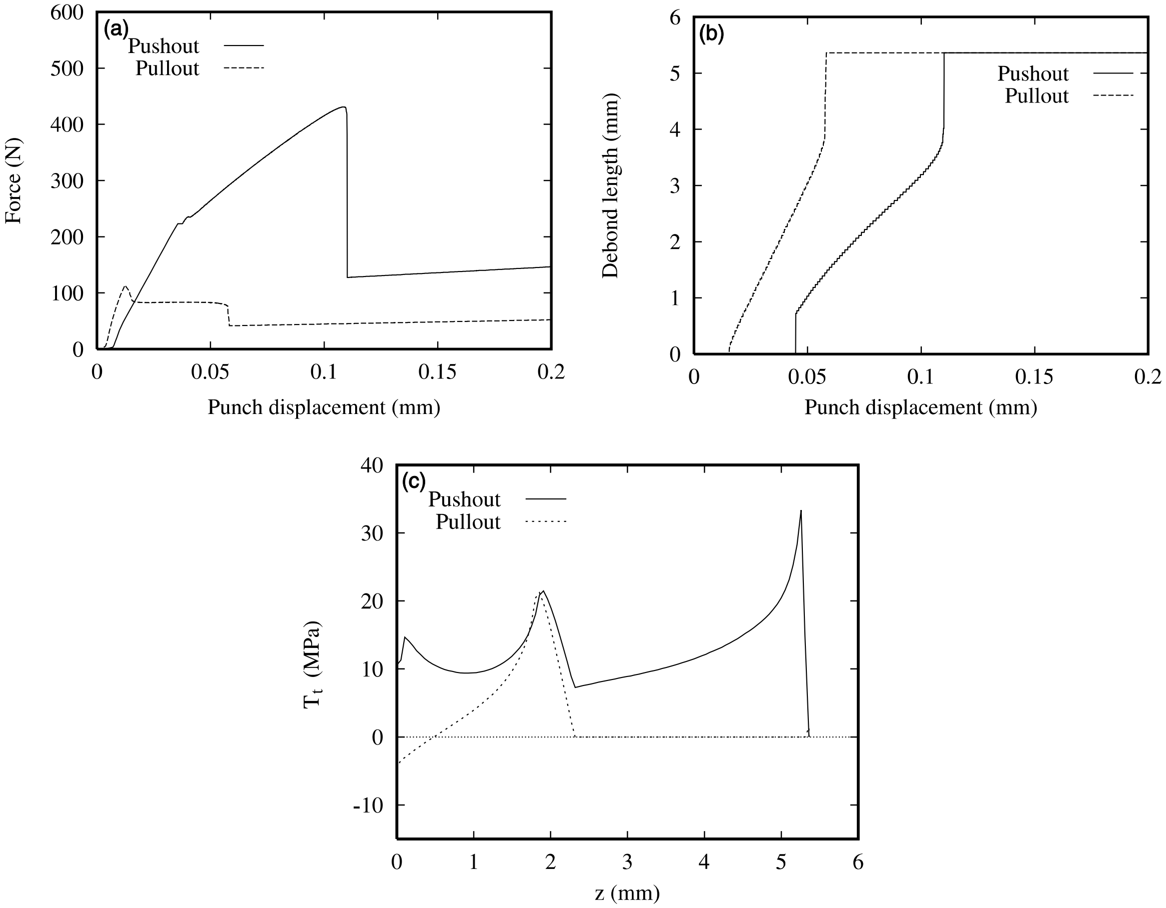

Fig. 12. Comparison of fiber pushout and pullout tests: (a) load versus punch displacement; (b) debond length versus punch displacement; (c) distribution of shear traction (T_t) along the interface for a debond length $L_c = 3$ mm.

of the interfacial shear stress (Fig. 12c). The geometry and material properties are the same as those used in Section 3.1. Note the drastic difference in deformation and failure behaviors: due to the absence of contact behind the advancing crack front, the pullout solution is much less stable and yields a maximum punch load equal to less than a quarter of that obtained in the pushout test.

It is worthnoting once again that the cohesive zone model is not limited to the prediction of interfacial failure. As indicated earlier, this phenomelogical failure model has been successfully used to describe a broad range of fracture processes in a wide variety of material systems. In order to have truly predictive capabilities, however, this type of failure model must rely on carefully designed and conducted experiments to extract the defining quantities (normal and shear strengths, critical displacement discontinuities, etc.).

Acknowledgements

This work has been performed as part of the ASCI Center for the Simulation of Advanced Rockets located at the University of Illinois at Urbana and funded by the US. Department of Energy through the University of California under Subcontract number B341494.

References

Atkinson, C., Avila, J., Betz, E., Smelser, R.E., 1982. The rod pull-out problem, theory and experiment. J. Mech. Phys. Solids 30 (3), 97–120.

Bechel, V., 1997. The application of debond length measurements to examine the accuracy of composite interface properties derived from fiber pushout testing. Ph.D Thesis, University of Illinois, Urbana, Champaign.

Bechel, V., Sottos, N.R., 1998a. Application of debond length measurements to examine the mechanics of fiber pushout. J. Mech. Phys. Solids 46, 1675–1697.

Bechel, V., Sottos, N.R., 1998b. A comparison of calculated and measured debond lengths from fiber pushout test. Comp. Sci. Technol. 58, 1727–1739.

Bechel, V., Sottos, N.R., 1998c. The effect of residual stresses and sample preparation on progressive debonding during the fiber pushout test. Comp. Sci. Technol. 58, 1741–1751.

Beckert, W., Lauke, B., 1995. Fracture mechanics finite element analysis of debonding crack extension for a single fibre pull-out specimen. J. Mater. Sci. Lett. 14, 333–336.

Bowling, J., Groves, G.W., 1979. The debonding and pull-out of ductile wires from a brittle matrix. J. Mater. Sci. 14, 431–442.

Camacho, G.T., Ortiz, M., 1996. Computational modelling of impact damage in brittle materials. Int. J. Solids Struct. 33 (20–22), 2899–2938.

Chandra, N., Ananth, C.R., 1995. Analysis of interfacial behavior in MMCs and IMCs by the use of thin-slice push-out tests. Comp. Sci. Technol. 54, 87–100.

Freund, L.B., 1991. The axial force needed to slide a circular fiber along a hole in an elastic material and implications for fiber pull-out. Eur. J. Mech. A/Solids 11, 1–19.

Geubelle, P.H., Baylor, J., 1998. Impact-induced delamination of laminated composites: a 2D simulation. Composites B 29, 589–602.

Hutchinson, J.W., Jensen, H.M., 1990. Models of fiber debonding and pullout in brittle composites with friction. Mech. Mat. 9, 139–163.

Kallas, M.N., Koss, D.A., Hahn, H.T., Hellman, J.R., 1992. Interfacial stress state present in a 'thin-slice' fiber push-out test. J. Mater. Sci. 27, 3821–3826.

Kendall, K., 1975. Model experiments illustrating fibre pull-out. J. Mater. Sci. 10, 1011–1014.

Kernas, R.J., Parthasarathy, T.A., 1991. Theoretical analysis of the fibre pullout and pushout tests. J. Amer. Ceram. Soc. 74 (7), 1585–1596.

Khanna, S.K., Shukla, A., 1994. Influence of fiber inclination and interfacial conditions on fracture in composite materials. Exper. Mech. 34 (2), 171–180.

Liang, C., Hutchinson, J.W., 1993. Mechanics of the fiber pushout test. Mech. Mat. 14, 207–221.

Lin, G., Cornec, A., Schwalbe, K.-H., 1998. Three-dimensional finite element simulation of crack extension in aluminum alloy 2024 FC. Fatigue Frac. Engng. Mater. Struct. 21, 1159–1173.

Lin, G., Kim, Y.-J., Cornec, A., Schwalbe, K.-H., 1997. Fracture toughness of a constrained metal layer. Comput. Mater. Sci. 9, 36–47.

McMeeking, R.M., Rice, J., 1975. Finite-element formulations for problems of large elastic–plastic deformation. Int. J. Solids Struct. 11, 601–616.

Needleman, A., 1987. A continuum model for void nucleation by inclusion debonding. J. Appl. Mech. 54 (3), 525–531.

Needleman, A., 1997. Numerical modeling of crack growth under dynamic loading conditions. Comput. Mech. 19 (6), 463–469.

Povirk, G.L., Needleman, A., 1993. Finite element simulations of fiber pull-out. J. Appl. Mech. 115, 286–291.

Shetty, D.K., 1988. Shear-lag analysis of fiber push-out (indentation) tests for estimating interfacial friction stress in ceramic–matrix composites. J. Am. Ceram. Soc. 71 (2), C107–C109.

Simo, J.C., Laursen, T.A., 1992. An augmented lagrangian treatment of contact problems involving friction. Comput. Struct. 42 (1), 97–116.

Tsai, K.-H., Kim, K.-S., 1996. The micromechanics of fiber pull-out. J. Mech. Phys. Solids 44 (7), 1147–1177.

Tvergaard, V., Hutchinson, J.W., 1992. The relation between crack growth resistance and fracture process parameters in elastic–plastic solids. J. Mech. Phys. Solids 40, 1377–1397.